Monthly Notices of the ROYAL ASTRONOMICAL SOCIETY

MNRAS **551,** 1–6 (2026) https://doi.org/10.1093/mnras/stag1646
Advance Access publication 2026 August 29

The magnetic field in M16: new results from the *JCMT* BISTRO survey

R. M. R. Tulloh ,[1★] D. Ward-Thompson,[1] J. Karoly,[1,2] J. M. Kirk[1] and K. Pattle [2]
[1]*Jeremiah Horrocks Institute, University of Lancashire, Preston PR1 2HE, UK*
[2]*Department of Physics and Astronomy, University College London, Gower Street, London WC1E 6BT, UK*

Accepted 2026 August 28. Received 2026 August 27; in original form 2026 June 30

ABSTRACT

We present a study of the magnetic field (B-field) in the Eagle Nebula (M16) using data from the *James Clerk Maxwell Telescope* B-fields In STar-forming Region Observations survey. We extend our previous study of the well-known 'Pillars of Creation' region of the nebula to study two other structures in the region, the 'Spire' and the bright-rimmed cloud known as 'SFO30'. These structures show similar B-field morphologies to the Pillars. We calculate B-field strengths using the Davis–Chandrasekhar–Fermi method and thereby estimate the magnetic potential energy in each of these regions for comparison with the local gravitational, turbulent, and thermal energies, as well as the pressure energy of the shocks from nearby O-type stars. We find approximate equipartition between the energies supporting the regions and those tending towards collapse, with the B-field support playing a significant role. This agrees with our earlier hypothesis that B-fields help support pillar-like structures in molecular clouds and make them longer-lived than they would otherwise have been.

Key words: stars: formation – ISM: individual objects: M16 – ISM: magnetic fields – submillimetre: ISM.

1 INTRODUCTION

The *Hubble Space Telescope* (*HST*) has taken many images, one of the most famous being the 'Pillars of Creation' in the Eagle Nebula. These photo-ionized pillars, or columns, are star-forming regions associated with nearby intermediate- to high-mass stars ($\gtrsim 8\,M_\odot$). K. Pattle et al. (2018) made the first detailed measurements of the magnetic field (B-field) in the densest parts of the Pillars, as part of the B-fields in STar-forming Region Observations (BISTRO) survey using the *James Clerk Maxwell Telescope (JCMT)* in Hawaii (D. Ward-Thompson et al. 2017). The present study aims to develop this work further.

W. A. Hiltner (1949) and J. S. Hall & A. H. Mikesell (1949) showed that the light that arose from areas with significant extinction was plane polarized. L. Davis & J. L. Greenstein (1951) proposed that it was dust grains that were responsible for this effect, but the mechanism was unclear and still remains an area of controversy. The Radiative Alignment Torque theory (A. Z. Dolginov & I. G. Mitrofanov 1976) proposed that anisotropic radiation fields exert torques on rotating asymmetric dust grains, leading to partial alignment of their angular momentum vectors. The grains precess about the ambient B-field direction. These grains are paramagnetic (containing silicates or iron) and above the critical size (10^{-6} m), below which rotation is primarily thermal (A. Lazarian 2007). The re-emission in the far-infra red spectrum results in partial linear polarization that is perpendicular to the B-field (A. Lazarian & T. Hoang 2008).

Young massive stars produce high-energy photons that ionize the surrounding parent molecular cloud, providing a shockwave that erodes the cloud (H. Zinnecker & H. W. Yorke 2007). Complex structures can form in the dense gas at the bow shock interfaces (L. Spitzer 1954), and particularly dense neutral columns, or pillars, can be seen protruding into photo-ionized regions, as in M16 (K. Pattle et al. 2018).

Submillimetre continuum polarization surveys represent a powerful technique for detecting B-field orientation and trying to understand its role in the star formation process within molecular clouds (D. Ward-Thompson et al. 2017). It is unclear whether the magnetic field stabilizes the dust and gas, or how it directs the accretion of the interstellar medium into the cores forming protostars, or what its role is in reducing star-forming efficiency (G. J. White et al. 1999; R. J. R. Williams, D. Ward-Thompson & A. P. Whitworth 2001; K. Pattle et al. 2023), but these are some of the questions that the BISTRO survey aims to address.

Fig. 1 shows the M16 region, known as the Eagle Nebula. On it are marked the positions of the 'Pillars', the young cluster of O- and B-type stars known as NGC 6611, the area mapped with SCUBA-2/POL-2 (white dashed circle), and the regions known as the 'Spire' and 'SFO30' – number 30 in the catalogue of Bright-Rimmed Clouds compiled by K. Sugitani, Y. Fukui & K. Ogura (1991), which appears to be not too dissimilar in shape and perhaps formation mechanism, to the 'Pillars'. Also labelled are two other regions that we looked at, known as 'I–II–III base' and 'IV base'. We have previously studied how the shock fronts from the nearby young high-mass cluster NGC 6611 photoionize and interact with the heads of the 'Pillars of Creation' (K. Pattle et al. 2018).

★ E-mail: rmrtulloh@lancashire.ac.uk

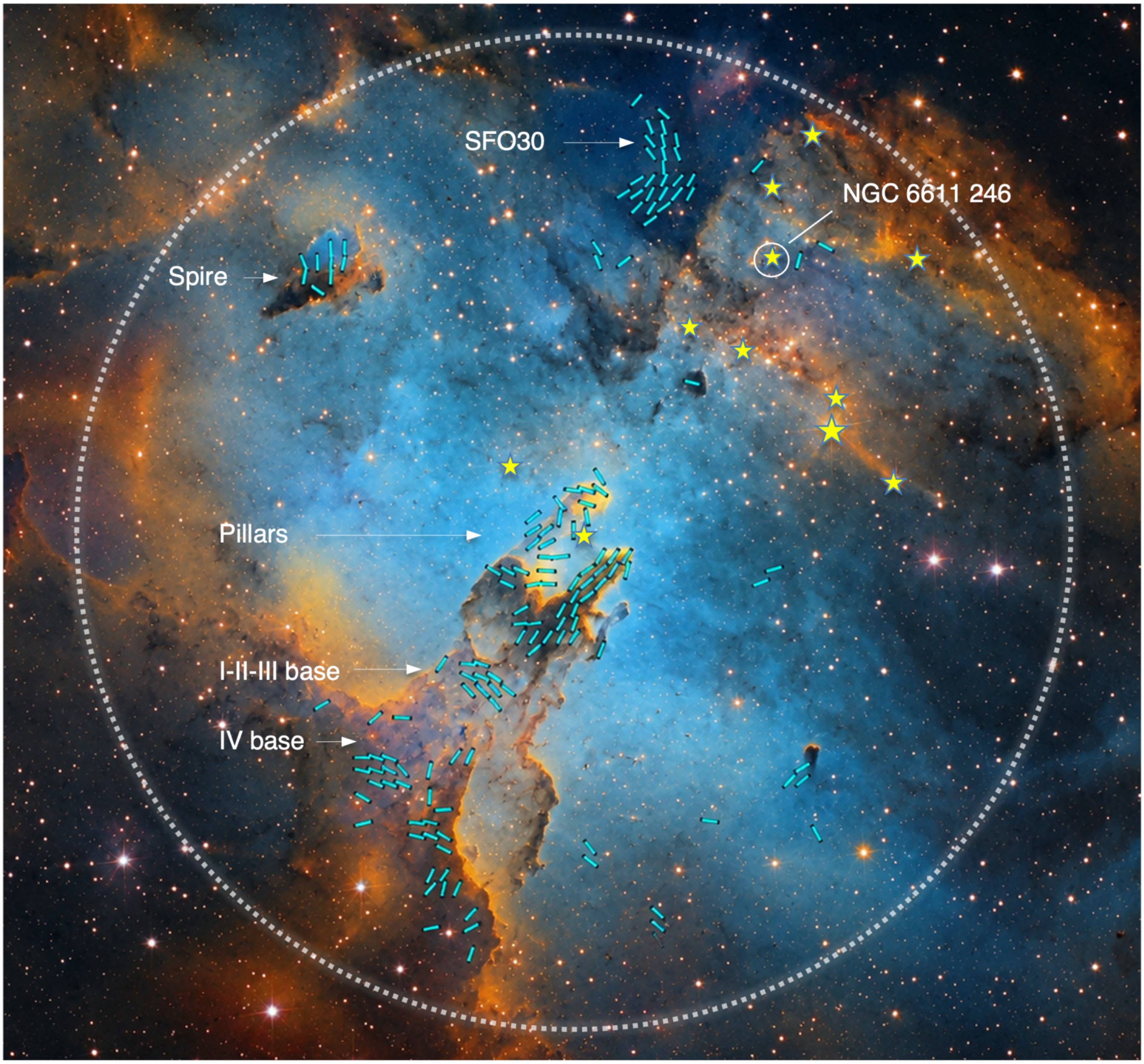

Figure 1. Wide-field view of the Eagle Nebula (M16), based on a recoloured DSS2 Blue image obtained from photographic plates from the *UK Schmidt Telescope*. The four regions of study: Spire, SFO30, I–II–III base, and IV base are labelled. Striped segments show the inferred plane-of-sky magnetic-field orientation derived from 850-μm dust polarization observations from the BISTRO survey, carried out with the *JCMT*. The dashed boundary indicates the approximate extent of the BISTRO-mapped region. Stars mark selected massive members of the ionizing cluster NGC 6611. The O7 II star NGC 6611 246 (BD−13°4927) is highlighted; its projected proximity to both the Spire and SFO30 suggests that it may contribute significantly to the local ionization and feedback environment within these structures.

This paper presents the results from the BISTRO survey of the wider M16 field, shown in Fig. 1, to examine other regions of the Eagle Nebula. We study the B-field deduced from the data and attempt to ascertain the role played by the B-field in this wider region.

2 OBSERVATIONS

We surveyed the Eagle Nebula, M16, at 850 μm with SCUBA-2 (W. S. Holland et al. 2013) and POL-2 (P. Friberg et al. 2016) between 2017 June 6 and 2017 July 27, under *JCMT* project code M17BL011.

The region was observed 20 times for ∼ 40 min each, giving a total on-source integration time of ∼ 14 h. The observations were made in the POL-2 DAISY mode, which produces a map with a high signal-to-noise ratio (SNR) in the central 3-arcmin-diameter region with increasing noise towards the edges (P. Friberg et al. 2016).

During the observations, which were taken in Band 2 weather, the atmospheric opacity, τ at 225 GHz, varied between ∼ 0.05 and

Table 1. Physical parameters of four regions in M16. Coordinates are centroid positions. B_{pos} is the derived magnetic field strength, using the compact DCF relation. σ_θ is the standard deviation of the polarization vector angles.

Region	α_{J2000} δ_{J2000}	Total mass ($M_{\text{T}}/\text{M}_\odot$)	σ_θ °	B_{pos} (μG)
Spire	18:19:08.011 −13:45:20.63	30 ± 5	24 ± 5	∼ 130–200
SFO 30	18:18:44.090 −13:44:07.97	38 ± 5	14 ± 5	∼ 260–350
I–II–III base	18:18:58.728 −13:51:41.50	15 ± 5	12 ± 5	∼ 130–200
IV base	18:19:01.024 −13:54:19.03	10 ± 5	18 ± 5	∼ 30–50

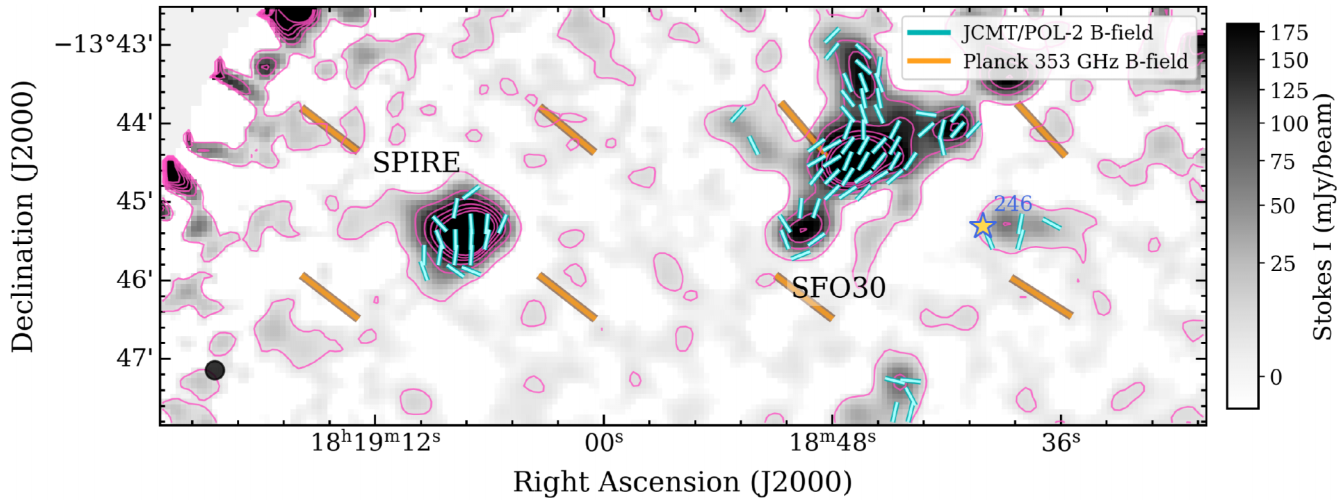

Figure 2. SCUBA-2 image of the Spire and SFO30 regions of the Eagle Nebula, M16. An ionizing star (NGC 6611 246) is also shown. The grey-scale shows the smoothed Stokes I 850-μm emission, while magenta contours mark increasing intensity levels and cyan bars show the inferred plane-of-sky B-field orientation. The longer, sparse orange bars are a visual guide to the large-scale magnetic-field orientation inferred from Planck 353-GHz Stokes Q and U data. The mean Planck magnetic-field position angle within a 30-arcmin aperture centred on M16 is 44.9 ± 1.6°, with a spatial angular dispersion of 15.3°. The mean *JCMT* field orientations are 1 ± 9° in the Spire and 138 ± 5° in SFO30, corresponding to axial offsets of 43.9 ± 9.1° and 86.9 ± 5.3°, respectively.

∼ 0.08 (K. Pattle et al. 2018). The effective beam size of the *JCMT* at 850 μm is 14.1 arcsec, or ∼ 0.1 pc at the distance of M16, which we take to be 1.74 ± 0.13 kpc (M. A. Kuhn et al. 2019).

The 850-μm data were reduced using the POL2MAP routine in the SMURF package in STARLINK. The standard reduction process is described in detail by K. Pattle et al. (2021). We adopted the 'August 2019' instrumental polarization (IP) model in order to correct for the IP in the Q and U maps. Table 1 lists the coordinates of the four main regions of study.

The final Stokes I, Q, U maps and the polarization catalogue are gridded to a default 4 arcsec pixel^{-1} scale. For the analysis, we follow K. Pattle et al. (2018), who used the *kappa* 'sqorst' command to rebin the I, Q, and U maps to a 14.1 arcsec pixel^{-1} scale (to match the beam size).

Independent polarization half-vectors are measured on a 14.1 arcsec pixel^{-1} scale, but the maps we show are of the B-field half-vectors, which are rotated by 90° relative to the polarization, while the Stokes I maps we use are at the default 4 arcsec pixel^{-1} scale. The survey observing strategy, data acquisition, reduction, and absolute calibration are discussed in more detail by D. Ward-Thompson et al. (2017).

3 DATA ANALYSIS

3.1 Magnetic field morphologies

Fig. 1 also shows an overlaid map of the B-field in those regions where we have sufficient SNR. The half-vectors show the direction of the B-field, since they are rotated by 90° relative to the measured polarization vectors. We mark the four additional regions we studied, which we label accordingly. The two regions at the base of the pillars are labelled 'I–II–III base' and 'IV base'. The other two are the 'Spire' and 'SFO30' regions mentioned above. Fig. 2 shows a close-up of the B-field maps of the latter two regions.

Fig. 1 reveals a range of B-field morphologies in the four mapped areas of the molecular cloud. K. Pattle et al. (2018) suggested that the magnetic field vectors in 'Pillar 2' are at right angles to a bow-shock that could be arising from the effects of the O-type star NGC 6611 205. We find the same vector orientation, but note that the O-type star NGC 6611 367 could also be the source of the bow-shock creating 'Pillar 2'.

Fig. 5 of K. Pattle et al. (2018) illustrates the proposed hypothesis that the B-field delays the erosion of the molecular cloud when an overdensity is encountered. The B-field is compressed and ordered by the presence of the shock front and supports the forming pillar against lateral erosion as seen in panel (c) of that figure.

In the region that we label 'I–II–III base', the field appears to be roughly as in the initial conditions in the Pattle model, since it is being shielded by the pillars. There is some evidence of the field turning at the edge, where it is less shielded.

The morphology of the B-field in the region we label 'IV base' is somewhat more complex. This region actually appears to be slightly foreground to the pillars. There is a region that is elongated parallel to the pillars, where the field appears to be parallel to the elongation and that might be a smaller version of 'Pillar 2'. At the base of this, there is a region of B-field roughly parallel to that in the 'I–II–III base' region. This then curves round to follow the edge of the cloud.

Fig. 2 shows a close-up view of the regions we call the Spire and SFO30. Once again we plot the magnetic field vectors that we have measured. The 'Spire' appears to be similar to a pillar, with B-field vectors at its tip being parallel to a putative bow-shock. This could possibly be arising from the influence of the nearest O-type star, NGC 6611 246, which lies at ~ 20 pc from M16 (based on its *Gaia* distance). The B-field vectors in the region we label 'SFO30' could also be interpreted as lying parallel to a putative ionizing front, also from NGC 6611 246.

Fig. 2 also shows the large-scale magnetic field, as measured by Planck. In the case of the Spire, we see that the small-scale field has rotated by roughly 45° relative to the large-scale field, and for SFO30 it has rotated by roughly 90°. Thus, the small-scale field has become dissociated from the large-scale field. This is consistent with the findings of Y. Doi et al. (2020), who found that there was a critical length scale, typically between the resolution of Planck and SCUBA-2, at which the magnetic field became structured and the small-scale field dissociated from the large-scale field.

3.2 Masses of regions of molecular cloud

The total (gas + dust) mass ($M_{\rm T}$) can be estimated from the dust mass by measuring the submillimetre flux density, (D. Ward-Thompson & A. P. Whitworth 2011), which traces the dust emission, and assuming a canonical dust-to-gas mass ratio of ~ 100, using equation (1):

$$M_{\rm T} = \frac{S_\nu D^2}{\kappa_{\nu(850)} B_\nu(T)}, \tag{1}$$

where S_ν is the integrated 850-µm flux density, D is the distance to M16, which we take to be 1.74 ± 0.13 kpc (M. A. Kuhn et al. 2019), and temperature $T = 20$ K (G. J. White et al. 1999; K. Pattle et al. 2021; J. Hwang et al. 2023). κ_ν is the gas-plus-dust mass opacity, which we take to be 0.00125 $\rm m^2\,kg^{-1}$ (K. Pattle et al. 2021), and $B_\nu(T)$ is the Planck function at $T = 20$ K. The total 850-µm flux density was integrated over an aperture of twice the full width calculated at half-maximum (FWHM) in each region to find the total mass, $M_{\rm T}$.

We measured the flux density, and re-calculated the mass, of 'Pillar 2'. We found it to be $35 \pm 5\ \rm M_\odot$, similar to that published by R. J. R. Williams et al. (2001), who obtained a value of 31 $\rm M_\odot$, within the uncertainties, giving us some confidence in our calibration. We went on to measure the other regions and calculate their masses, and we list these in Table 1.

3.3 Magnetic field strengths

The Davis–Chandrasekhar–Fermi, or DCF, method (L. Davis 1951; S. Chandrasekhar & E. Fermi 1953) takes an estimate of the ratio of the non-thermal velocity dispersion to the dispersion in the magnetic field direction as a proxy for the magnetic field strength. The two dispersions can be measured, and this provides an estimate of the plane-of-sky B-field strength, $B_{\rm pos}$ (K. Pattle et al. 2018). In full, this is given by

$$B_{\rm pos} = Q\sqrt{(4\pi\rho)}\frac{\sigma_v}{\sigma_\theta} \approx 9.3\sqrt{n({\rm H}_2)}\frac{\Delta v}{\sigma_\theta}\mu{\rm G}\,, \tag{2}$$

where the terms have the following meanings: Q is a factor that accounts for variation in the field on scales smaller than the beam and we take a value of 0.5 ± 0.1 (E. C. Ostriker, J. M. Stone & C. F. Gammie 2001; R. M. Crutcher 2012); ρ is the gas density of each dense core, which we have converted to hydrogen number density, $n({\rm H}_2)$, assuming assuming that the core is spherical and that μ, which is the mean molecular weight, is 2.8 (R. M. Crutcher et al. 2004; J. Kauffmann et al. 2008); $m_{\rm H}$ is the mass of the hydrogen atom. σ_v is the non-thermal gas velocity dispersion and Δv is the FWHM of the velocity, assuming a Gaussian velocity distribution, for which we take a value of 0.8–1.2 km $\rm s^{-1}$ (G. J. White et al. 1999; K. Pattle et al. 2018; R. K. Friesen et al. 2017); σ_θ is the standard deviation of the polarization angle about the mean field direction, listed in Table 1. Using equation (2), we calculate $B_{\rm pos}$ in each of the four regions, and list these in Table 1. Note that there are large uncertainties associated with this method (C.-Y. Chen et al. 2022). A limitation of the DCF analysis is that the angular dispersion measured from the POL-2 vectors samples the plane-of-sky structure, whereas the velocity dispersion is measured along the line of sight. The DCF estimate therefore assumes that the gas contributing to the adopted linewidth samples a depth comparable to the region over which the polarization angles are measured; if unrelated material along the line of sight contributes significantly to the linewidth, the derived magnetic-field strength may be overestimated. We believe the latter to be unlikely, but for this reason, we treat the DCF field strengths as approximate, order-of-magnitude estimates rather than precise measurements.

4 ENERGY BALANCE

4.1 Criticality

The virial theorem equates the different forms of potential energy in a system and requires them to balance for the system to be in equilibrium. In this case, the relevant energies are the thermal dynamical potential energy ($E_{\rm T}$), the non-thermal (or turbulent) dynamical potential energy ($E_{\rm NT}$), the magnetic potential energy ($E_{\rm B}$), the gravitational potential energy ($E_{\rm G}$), and the potential energy of the ionizing radiation pressure ($E_{\rm X}$) from the nearby O-type stars (D. Ward-Thompson et al. 2006). The first three act to support a core, whereas the last two act to make a core collapse, and so the relation between them all tells us about the stability of a core. This is known as magnetic criticality. Consequently, for equilibrium we require that

$$2E_{\rm T} + 2E_{\rm NT} + E_{\rm B} \approx E_{\rm G} + E_{\rm X}. \tag{3}$$

If the right-hand side (RHS) is significantly greater than the left-hand side (LHS), we say that the core is super-critical, and we predict that the core will collapse. If it is significantly less than the

Table 2. Virial energy balance of the 'Spire' and 'SFO30' M16 regions. For equilibrium, the sum of the top three rows (the LHS of equation 3) should roughly equal the sum of the lower two rows (the RHS of equation 3).

Parameter	Spire / 10^{37} J	SFO30 / 10^{37} J
$2E_T$	$\sim$ 1.1–1.5	$\sim$ 1.4–2.1
$2E_{NT}$	$\sim$ 2.1–4.7	$\sim$ 2.6–5.9
E_B	$\sim$ 0.5–1.2	$\sim$ 1.8–4.1
E_G	$\sim$ 5.4–7.2	$\sim$ 8.4–10.3
E_X	$\sim$ 0.1–0.3	$\sim$ 0.1–0.3
LHS	$\sim$ 3.7–7.4	$\sim$ 5.8–12.1
RHS	$\sim$ 5.5–7.5	$\sim$ 8.5–10.6

LHS, then we say that the core is sub-critical, and we predict that the core will expand. The equality leads to approximate stability and equilibrium. The terms in this equation are given by

$$2E_T = \frac{3Mk_BT}{\mu m_H}, \quad (4)$$

$$2E_{NT} = \frac{3M\Delta v^2}{8\ln(2)}, \quad (5)$$

$$E_B = \frac{B^2V}{2\mu_0}, \quad (6)$$

$$E_G = \frac{\eta GM^2}{R}, \quad (7)$$

$$E_X = \frac{4R^2k_BT_{\rm II}}{D} \times \left(\frac{3\pi NR}{\alpha_*}\right)^{1/2}, \quad (8)$$

(D. Ward-Thompson et al. 2006), where symbols have the following meanings: R is the core radius, $T_{\rm II}$ is the canonical temperature of the ionized H II region (we take 10^4 K), and N is the photon rate of the ionizing star.

We calculate that the nearest ionizing star to both the 'Spire' and 'SFO30' is NGC 6611 246 (aka BD-13°4927), which, according to its *Gaia* DR3 distance, is $\sim$ 20 pc from both (Gaia Collaboration 2016). It is an O7 II star, so we can estimate N to be $\sim 3 \times 10^{47}$ to 3×10^{48} s^{-1} (D. Schaerer & A. de Koter 1997; O. G. Telford et al. 2023). α_* is the recombination coefficient for atomic hydrogen into excited states only (2×10^{-19} m^3 s^{-1}). η is the coefficient determined by the density profile of the core, where we take $\eta =$ 0.6–0.8 to allow for different density profiles (A. P. Whitworth & D. Ward-Thompson 2001; D. Ward-Thompson et al. 2006). In the calculation of $2E_T$ we allow for a range of values of T of up to $\sim$ 30 K.

Following previous analyses in BISTRO publications, we adopt the one-dimensional velocity dispersion σ_v corresponding to a Gaussian line profile, for which Δv is the FWHM. μ is the mean molecular weight, which we take to be 2.8, as stated above (R. M. Crutcher et al. 2004; J. Kauffmann et al. 2008), whereas μ_0 is the magnetic permeability of free space.

The two regions that we labelled 'base' are clearly just parts of the attached pillars that have been well studied previously. Therefore, for the remainder of this paper we concentrate on the regions we refer to as the 'Spire' and 'SFO30'. For both of these regions, we carry out the calculations listed in equations (4)–(8) and list the values that we obtain in Table 2.

4.2 The spire

We first concentrate on the region referred to as the 'Spire'. We note that, if we substitute the values from Table 2 into equation (3), we obtain a range of values for the LHS of $\sim$ 3.7–7.4, while the RHS has a range of values of $\sim$ 5.5–7.5. These two ranges are essentially the same (given the size of the uncertainties), as per the requirement for equilibrium, with the RHS simply having a narrower range due to the range of uncertainties in the input values. It is notable that all energies have the same order of magnitude.

This also leads us to the hypothesis that this may be a bound core and hence could be termed 'pre-stellar', rather than merely 'starless' (D. Ward-Thompson et al. 1994). However, we also note that the contribution of E_B to the 'supporting' potential energies, is in the range $\sim$ 15–20 per cent, which we claim is significant.

Consequently, we propose that the tip of the Spire contains a pre-stellar core in approximate virial equilibrium and that the magnetic field is playing a significant role in maintaining that equilibrium. This is similar to the findings of K. Pattle et al. (2018) in the 'Pillars of Creation' – particularly at the head of 'Pillar 2'.

4.3 SFO30

Now turning to 'SFO30', we note that the LHS of equation (3) in this case is $\sim$ 5.8–12.1, while the RHS is $\sim$ 8.5–10.6. Hence, the range of potential energies of the forces trying to collapse the core lies entirely within the range of those trying to support the core.

We interpret this as another core that is probably bound, but lying in approximate equilibrium. Once again the magnetic field appears to play a significant role, contributing $\sim$ 30 per cent of the LHS. Hence, it is being supported significantly by magnetic pressure as well as gas pressure, against its own self-gravity and the external pressure of nearby O-type stars, while remaining bound.

5 SUMMARY

We have mapped the wider region of the Eagle Nebula, M16, in 850-μm polarized dust emission as part of the *JCMT* BISTRO survey, using the SCUBA-2/POL-2 polarimeter-camera combination. We covered not only the region of the 'Pillars of Creation', but also the wider nebula, including in particular regions known as the 'Spire' and the bright-rimmed cloud that we refer to as 'SFO30'.

We note that both the 'Spire' and 'SFO30' display a magnetic field pattern that mimics the field pattern seen in the 'Pillars'. Namely, the field lies along the length of the pillars and curves around at their tips. 'SFO30' shows both the longitudinal field and the curving round at the tip. Whereas the 'Spire' only shows the region where the field at the tip lies orthogonal to the direction to the O-type star that is causing the pillar-like structure, just like 'Pillar 1'.

We find agreement with the formation model of the pillars proposed by K. Pattle et al. (2018), in which a shock from a nearby O-type star erodes a cloud around a pre-existing overdensity in the cloud and creates a pillar with a dense core at its tip. During this process, the pre-existing magnetic field is forced to lie along the length of the pillar, curving round at its tip. Both the 'Spire' and 'SFO30' demonstrate this behaviour.

The POL-2 magnetic-field orientations were compared with the larger-scale magnetic-field direction inferred from Planck 353-GHz Stokes Q and U data, as shown in Fig. 2. This suggests that the dense-gas field is locally reoriented rather than simply tracing the surrounding Galactic-scale field.

We used the DCF method to estimate the magnetic field strength in these regions, based on the angular dispersion of the polarization vectors. We estimated the magnetic potential energy in each region and compared it to the pressure energy of the gas (both thermal and non-thermal) and the potential energy of each core's self-gravity, as well as the external pressure exerted by nearby O-type stars.

Based on this analysis, we found that both the 'Spire' and 'SFO30' are in approximate equilibrium. In both cases, the magnetic field contributes significantly to the support of the cores, just as was previously found in the pillars.

Consequently, we support the previous conclusion that the pillars are magnetically supported and postulate that the previous model for their development is correct. Furthermore, we showed that the pillars are not unique, and here we suggest that this might be a fairly common star formation mechanism. Hence, we propose that cores formed in this way are longer-lived than they would otherwise have been, courtesy of the support of their internal magnetic fields.

ACKNOWLEDGEMENTS

DW-T and JMK acknowledge the Science and Technology Facilities Council (STFC) support under grant number ST/R000786/1. KP is a Royal Society University Research Fellow, supported by grant number URF/R1/211322. JK is currently supported by the Royal Society under grant number RF\ERE\231132, as part of project URF\R1\211322. The *JCMT* is operated by the East Asian Observatory on behalf of the Academia Sinica Institute of Astronomy and Astrophysics, and the National Astronomical Research Institute of Thailand. Additional funding support is provided by the Science and Technology Facilities Council of the United Kingdom and participating universities in the United Kingdom and Canada. The authors wish to recognize and acknowledge the very significant cultural role and reverence that the summit of Maunakea has always had within the indigenous Hawaiian community. We are most fortunate to have the opportunity to conduct observations from this mountain.

SCUBA-2 and POL-2 were built at the UK Astronomy Technology Centre, partially through grants from the Canada Foundation for Innovation. This research used the facilities of the Canadian Astronomy Data Centre operated by the National Research Council of Canada with the support of the Canadian Space Agency. This research has also made use of NASA's Astrophysics Data System Bibliographic Services, and distances were obtained using data from the European Space Agency (ESA) mission *Gaia* (https://www.cosmos.esa.int/gaia), processed by the *Gaia* Data Processing and Analysis Consortium (DPAC, https://www.cosmos.esa.int/web/gaia/dpac/consortium). Funding for the DPAC has been provided by national institutions, in particular the institutions participating in the *Gaia* Multilateral Agreement.

DATA AVAILABILITY

All data are available through the Canadian Astrophysics Data Centre (CADC).

REFERENCES

Chandrasekhar S., Fermi E., 1953, ApJ, 118, 113
Chen C.-Y., Li Z.-Y., Mazzei R. R., Park J., Fissel L. M., Chen M. C.-Y., Klein R. I., Li P. S., 2022, MNRAS, 514, 1575
Crutcher R. M., 2012, ARA&A, 50, 29
Crutcher R. M., Nutter D. J., Ward-Thompson D., Kirk J. M., 2004, ApJ, 600, 279
Davis L., 1951, Phys. Rev., 81, 890
Davis L. Jr, Greenstein J. L., 1951, ApJ, 114, 206
Doi Y. et al., 2020, ApJ, 899, 28
Dolginov A. Z., Mitrofanov I. G., 1976, Ap&SS, 43, 291
Friberg P., Bastien P., Berry D., Savini G., Graves S. F., Pattle K., 2016, in Holland W. S., Zmuidzinas J., eds, Proc. SPIE Conf. Ser. Vol. 9914, Millimeter, Submillimeter, and Far-Infrared Detectors and Instrumentation for Astronomy VIII. SPIE, Bellingham, p. 991403
Friesen R. K. et al., 2017, ApJ, 843, 63
Gaia Collaboration, 2016, A&A, 595, A1
Hall J. S., Mikesell A. H., 1949, AJ, 54, 187
Hiltner W. A., 1949, Science, 109, 165
Holland W. S. et al., 2013, MNRAS, 430, 2513
Hwang J., Pattle K., Parsons H., Go M., Kim J., 2023, AJ, 165, 198
Kauffmann J., Bertoldi F., Bourke T. L., Evans N. J. II, Lee C. W., 2008, A&A, 487, 993
Kuhn M. A., Hillenbrand L. A., Sills A., Feigelson E. D., Getman K. V., 2019, ApJ, 870, 32
Lazarian A., 2007, J. Quant. Spec. Radiat. Transfer, 106, 225
Lazarian A., Hoang T., 2008, ApJ, 676, L25
Ostriker E. C., Stone J. M., Gammie C. F., 2001, ApJ, 546, 980
Pattle K. et al., 2018, ApJ, 860, L6
Pattle K. et al., 2021, ApJ, 907, 88
Pattle K., Fissel L., Tahani M., Liu T., Ntormousi E., 2023, in Inutsuka S., Aikawa Y., Muto T., Tomida K., Tamura M., eds, ASP Conf. Ser. Vol. 534, Protostars and Planets VII. Astron. Soc. Pac., San Francisco, p. 193
Schaerer D., de Koter A., 1997, A&A, 322, 598
Spitzer L. Jr, 1954, ApJ, 120, 1
Sugitani K., Fukui Y., Ogura K., 1991, ApJS, 77, 59
Telford O. G., McQuinn K. B. W., Chisholm J., Berg D. A., 2023, ApJ, 943, 65
Ward-Thompson D., Whitworth A. P., 2011, An Introduction to Star Formation. Cambridge University Press, Cambridge, UK
Ward-Thompson D., Scott P. F., Hills R. E., Andre P., 1994, MNRAS, 268, 276
Ward-Thompson D., Nutter D., Bontemps S., Whitworth A., Attwood R., 2006, MNRAS, 369, 1201
Ward-Thompson D. et al., 2017, ApJ, 842, 66
White G. J. et al., 1999, A&A, 342, 233
Whitworth A. P., Ward-Thompson D., 2001, ApJ, 547, 317
Williams R. J. R., Ward-Thompson D., Whitworth A. P., 2001, MNRAS, 327, 788
Zinnecker H., Yorke H. W., 2007, ARA&A, 45, 481

This paper has been typeset from a TEX/LATEX file prepared by the author.